Cancer Letters 613 (2025) 217512

Contents lists available at ScienceDirect

Cancer Letters

journal homepage: www.elsevier.com/locate/canlet

Original Articles

Acidosis overrides molecular heterogeneity to shape therapeutically targetable metabolic phenotypes in colon cancers

Elena Richiardone [a], Maria Virginia Giolito [a], Rim Al Roumi [a], Jérôme Ambroise [b], Romain Boidot [c], Bernhard Drotleff [d], Bart Ghesquière [e,f], Barbara Lupo [g,h], Livio Trusolino [g,h], Alberto Bardelli [i,j], Sabrina Arena [g,h], Olivier Feron [a,k], Cyril Corbet [a,k,*]

[a] Pole of Pharmacology and Therapeutics (FATH), Institut de Recherche Expérimentale et Clinique (IREC), UCLouvain, Avenue Hippocrate 57, B1.57.04, B-1200, Brussels, Belgium
[b] Centre des Technologies Moléculaires Appliquées (CTMA), Institut de Recherche Expérimentale et Clinique (IREC), UCLouvain, Avenue Hippocrate 54, B-1200, Brussels, Belgium
[c] Unit of Molecular Biology, Department of Biology and Pathology of Tumors, Georges-François Leclerc Cancer Center-UNICANCER, 21079, Dijon, France
[d] Metabolomics Core Facility, EMBL Heidelberg, Heidelberg, Germany
[e] Laboratory of Applied Mass Spectrometry, Department of Cellular and Molecular Medicine, KU Leuven, Leuven, Belgium
[f] Metabolomics Core Facility Leuven, Center for Cancer Biology, VIB, Leuven, Belgium
[g] Department of Oncology, University of Torino, Candiolo (TO), Italy
[h] Candiolo Cancer Institute - FPO IRCCS, Candiolo (TO), Italy
[i] Department of Oncology, Molecular Biotechnology Center, University of Torino, Torino, Italy
[j] IFOM ETS, The AIRC Institute of Molecular Oncology, 20139, Milan, Italy
[k] WEL Research Institute, Avenue Pasteur 6, B-1300, Wavre, Belgium

ARTICLE INFO

Keywords:
Colon cancer
Acidosis
Metabolism
Microenvironment
PHGDH
Mitochondrial respiration

ABSTRACT

Colorectal cancer (CRC) represents a prototypical example of a cancer type for which inter- and intra-tumor heterogeneities remain major challenges for the clinical management of patients. Besides genotype-mediated phenotypic alterations, tumor microenvironment (TME) conditions are increasingly recognized to promote intrinsic diversity and phenotypic plasticity and sustain disease progression. In particular, acidosis is a common hallmark of solid tumors, including CRC, and it is known to induce aggressive cancer cell phenotypes. In this study, we report that long-term adaptation to acidic pH conditions is associated with common metabolic alterations, including a glycolysis-to-respiration switch and a higher reliance on the activity of phosphoglycerate dehydrogenase (PHGDH), in CRC cells initially displaying molecularly heterogeneous backgrounds. Pharmacological inhibition of PHGDH activity or mitochondrial respiration induces greater growth-inhibitory effects in acidosis-exposed CRC cells in 2D and 3D culture conditions, and in patient-derived CRC organoids. These data pave the way for drugs targeting the acidic tumor compartment as a "one-size-fits-all" therapeutic approach to delay CRC progression.

1. Introduction

Colorectal cancer (CRC) represents the third most common cancer in developed countries and is a leading cause of cancer-related deaths worldwide [1]. While clinical management of CRC patients is largely determined by pathological examination of tumor specimens (i.e., biopsy, polypectomy, or surgical resection), molecular testing plays an increasingly important role in the era of personalized medicine for patients with metastatic CRC [2]. Indeed, in the metastatic setting, genetic profiling for *RAS/BRAF* and immunohistochemistry-based assessment of mismatch repair/microsatellite instability (MSI) are routinely applied to guide the use of anti-EGFR targeted therapy and immune checkpoint inhibitors, respectively [3]. Nevertheless, CRC is a heterogeneous group of diseases with distinct morphological, molecular, and clinical features, and the prognosis for CRC patients remains very poor due to therapy resistance and disease progression. A gene

* Corresponding author. Pole of Pharmacology and Therapeutics (FATH), Institute de Recherche Expérimentale et Clinique (IREC), UCLouvain, Avenue Hippocrate 57, B1.57.04, B-1200, Brussels, Belgium.
E-mail address: cyril.corbet@uclouvain.be (C. Corbet).

https://doi.org/10.1016/j.canlet.2025.217512
Received 4 November 2024; Received in revised form 20 January 2025; Accepted 28 January 2025
Available online 1 February 2025

expression-based classification of CRC into four consensus molecular subtypes (CMS) has contributed, in the last decade, to a better understanding of inter-patient heterogeneity and prognosis [4], but without modifying the clinical routine yet. A major clinical challenge for CRC patients resides in the intratumoral heterogeneity that can manifest at (epi)genomic, transcriptomic, and proteomic levels [5]. Indeed, several studies have carried out single-cell dissection of CRC to reveal intra-cancer diversification, with various mutational signatures, methylome and transcriptome patterns, and distinct responses to conventional anticancer treatments [6–9].

Tumor microenvironment (TME) is thought to strongly contribute to genomic and phenotypic intratumoral heterogeneity in CRC [10]. For instance, glucose deprivation has been reported as a strong selection pressure for mutated *KRAS* in CRC cells [11]. Acidosis is a common hallmark of solid cancers, including CRC, and acidosis-based imaging modalities have recently emerged as promising strategies to improve CRC detection, surveillance, and staging [12–14]. Acidosis is known to contribute to the genetic instability of tumor cells [15,16], and to profoundly alter their transcriptomic profile [17]. Extracellular acidic pH has also been reported to sustain a more aggressive cancer cell phenotype, by favoring a slow-proliferating, stem-like, and pro-invasive cell state [18,19]. We and others have documented an increased autophagic flux [20] and a metabolic addiction towards exogenous fatty acids [21–24] in cancer cells upon chronic adaptation to acidic pH conditions.

In this study, we reason that chronic exposure to an acidic TME may override molecular heterogeneity in CRC cells to shape common metabolic traits that may be therapeutically exploited, as a "one-size-fits-all" approach to thwart acidosis-induced cancer cell aggressiveness. We report a shift from glycolysis to mitochondrial respiration as a consistent metabolic alteration in acidosis-adapted CRC cells, regardless of their genetic background and basal metabolic profile. We further reveal that these cells strongly depend on the activity of phosphoglycerate dehydrogenase (PHGDH), the rate-limiting enzyme of the serine biosynthesis pathway, to sustain their aggressiveness. Finally, we document that pharmacological inhibition of PHGDH or oxidative phosphorylation (OXPHOS) significantly reduces the viability of acidosis-exposed CRC cells, as well as the growth of patient-derived CRC models.

2. Materials and methods

2.1. Cell lines and culture

HCT-116 (#CCL-247) and HT-29 (#HTB-38) human colon cancer cell lines were purchased from the American Type Culture Collection (ATCC). DiFi and LIM1215 human colon cancer cell lines were obtained from Prof Alberto Bardelli, University of Torino, Italy, with permission from the Ludwig Institute for Cancer Research, Zurich, Switzerland. The LIM1215 cell line had been described previously [25]. Cell lines were stored according to the supplier's instructions and used within 6 months after resuscitation of frozen aliquots. All cell lines were maintained in Dulbecco's Modified Eagle Medium (#D5030, Sigma-Aldrich) supplemented with 10 % heat-inactivated fetal bovine serum (FBS; F7524, Sigma-Aldrich), 10 mM D-glucose (#G8270, Sigma-Aldrich), 2 mM L-glutamine (#25030-024, Thermo Fisher Scientific), 1 % penicillin-streptomycin (#15140163, Thermo Fisher Scientific) and 25 mM of both PIPES (#P1851, Sigma-Aldrich) and HEPES (#H3375, Sigma-Aldrich) before adjusting pH to 7.4 or 6.5. Acidic pH-adapted tumor cells were established as previously described [22,23]. All cell lines were maintained in exponential growth in 5 % CO_2/95 % air in a humidified incubator at 37 °C and then tested for mycoplasma contamination with the PCR-based MycoplasmaCheck service from Eurofins Genomics.

2.2. Cell treatment and transfection

Cells were seeded (5×10^4 cells/well; ≥3 wells/condition) in 96-well plates in a routine culture medium. The day after, cell treatment was performed in routine culture medium with NCT-503 (#SML1659, Sigma-Aldrich) or IACS-010759 (#HY-112037, MedChemExpress) for 72h at different concentrations, as indicated in the figure legends. In some conditions, cells were cultured in a serine-deprived culture medium, with or without supplementation with 0.21 g/L L-serine (#S4311, Sigma-Aldrich). Cell growth was assessed either by direct cell counting on a hemocytometer with Trypan Blue exclusion dye or by using the Presto Blue reagent (#A13262; Thermo Fisher Scientific) according to the manufacturer's instructions.

Cell transfection with 50 nM of either a non-targeting pool of 4 siRNA sequences (D-001810-10-05) or a pool of 4 siRNA sequences targeting human PHGDH (L-009518-00-0005), all from Horizon Discovery, was carried out with Lipofectamine™ RNAiMAX transfection reagent (#13778150; Thermo Fisher Scientific), according to manufacturer's instructions.

2.3. Western blot analysis

Subconfluent cancer cells were washed twice with ice-cold PBS and lysed in a RIPA buffer supplemented with phosphatase and protease inhibitor cocktails (#4906837001 and P8340, Sigma-Aldrich). Cell lysates were then cleared by centrifugation (6000×*g*, 10 min, 4 °C) and stored at −80 °C until analysis. After determination of protein concentration using a bicinchoninic acid-based assay (Thermo Fisher Scientific), samples were denaturated (5 min, 95 °C) with Laemmli sample buffer containing 100 mM dithiothreitol. Samples (20 µg per well) were then separated by SDS-PAGE (8 % acrylamide/bis-acrylamide gels) and transferred to PVDF membranes. Membranes were blocked with 5 % bovine serum albumin (BSA) in TBS-0.1 % Tween 20 (TTBS) and subsequently immunoblotted overnight at 4 °C with specific primary antibodies against PHGDH (#66350, Cell Signaling Technology, 1:1000), PSAT1 (#NBP1-32920, Novus Biologicals, 1:1000), PSPH (#58258, Cell Signaling Technology, 1:1000), SHMT1 (#41107, Cell Signaling Technology, 1:1000), SHMT2 (#33443, Cell Signaling Technology, 1:1000) or Hsp90 (#610419, BD Biosciences, 1:10,000). After several washes with TTBS, membranes were then incubated (1h, room temperature (RT)) with horseradish peroxidase (HRP)-conjugated secondary antibodies (Jackson Immunoresearch) and chemoluminescent signals were revealed by using ECL Western Blotting Detection Kit (GE Healthcare) on X-ray films in a dark chamber or with an Amersham Imager 600 (GE Healthcare).

2.4. RNA extraction and RT-qPCR

Subconfluent cancer cells were washed twice with ice-cold PBS and harvested in Tri-Reagent (Molecular Research Center). RNA was recovered after separation in 1-bromo-3-chloropropane and precipitation with isopropanol, washed with 70 % ethanol, resuspended in RNase-free water, and then quantified by spectrophotometry (Nanodrop 1000, Thermo Fisher Scientific). After reverse transcription on 1 µg of total RNA with the RevertAid Reverse-Transcriptase, oligo-dT and random hexamers (Thermo Fisher Scientific), quantitative PCR amplification was performed on a ViiA 7 real-time PCR system (Applied Biosystems) using SYBR® select master mix for cfx (Thermo Fisher Scientific) and gene-specific primer sequences for human *PHGDH* (*PHGDH*-Fw: CTTACCAGTGCCTTCTCTCCAC, *PHGDH*-Rv: GCTTAGGCAGTTCCCAGCATTC, amplicon size: 153 bp) or human *RPLP0* as reference gene (*RPLP0*-Fw: AGCCCAGAACACTGGTCTC, *RPLP0*-Rv: ACTCAGGATTTCAATGGTGCC, amplicon size: 97 bp). Data were analyzed according to ddCt method.

2.5. Dosage of extracellular glucose and lactate

Cancer cells (2×10^5 cells/well; 3 wells/condition) were seeded in 12-well plates with 1 mL of their routine culture medium. After 24h, the

medium was replaced by 500 μL of DMEM containing 10 mM D-glucose (#G8270, Sigma-Aldrich) and supplemented with 2 mM L-glutamine and 10 % dialyzed FBS (#F0392, Sigma-Aldrich). Initial concentrations of glucose and lactate in the experimental medium were also assessed by including control wells containing only cell culture medium (no cells) on each plate. After incubation for 24h, extracellular media were collected and deproteinized by centrifugation (15 min, 10,000 rpm, 4 °C) in 10 kDa cut-off filter tubes (VWR). Glucose and lactate concentrations were measured in the samples (50 μL) by using enzymatic assays (CMA Microdialysis AB) and an ISCUSflex microdialysis analyzer (Aurora Borealis). Data analysis was done by calculating the difference in glucose and lactate concentrations between the control wells and the experimental wells. Data were then normalized by the protein content in each well and expressed in μmol/hr/mg protein.

2.6. Seahorse analysis

Oxygen consumption rate (OCR) and extracellular acidification rate (ECAR) were measured by using the Seahorse XFe96 plate reader (Agilent). All assays were carried out using a seeding density of 3×10^4 cells/well in non-buffered DMEM, adjusted at pH 7.4 or 6.5 according to the cell lines. Mitochondrial respiration and glycolytic capacities were assessed by using the XF Cell Mito Stress Test and XF Glycolysis Stress Test, respectively, according to the manufacturer's recommendations. Briefly, mitochondrial function parameters (i.e. basal and maximal respirations) were evaluated in a DMEM medium containing 10 mM glucose and 2 mM glutamine and after sequential treatment with 1 μM oligomycin, 1 μM carbonyl cyanide-4 (trifluoromethoxy)phenylhydrazone (FCCP) and 0.5 μM rotenone/antimycin A. Glycolytic function was assessed in a DMEM medium containing 2 mM glutamine and after sequential treatment with 10 mM glucose, 1 μM oligomycin and 50 mM 2-DG. Glucose-dependent ECAR was calculated by comparing the values before and after the addition of the substrate. Data were normalized by the protein content in each well and expressed in mpH/min/μg protein (ECAR) or pmoles/min/μg protein (OCR).

2.7. Untargeted metabolomics

Cancer cells were seeded (3×10^6 cells/dish; 3 dishes/condition) in 60-mm dishes in routine culture medium for 72h (with medium renewal after 48h). The medium was then removed, and cells were washed with ice-cold PBS. Dishes were kept from this step on dry ice. Ice-cold methanol 80 % (v/v) was added to each dish (4 mL/dish) and incubated for 20 min at −80 °C. Cells were scraped and transferred to 5 mL Eppendorf tubes pre-cooled in dry ice. Metabolomics standard mix 1 (#MSK-MET1-1; Cambridge Isotope Laboratories), used as an internal standard for untargeted metabolomics, was added to each sample (1.2 μL/sample) which was then directly stored at −80 °C until processing. For further homogenization, zirconia/glass beads (1.0 mm; Biospec Products) were added to the quenched cell suspension, and samples were processed on dry ice via a bead beater (FastPrep-24; MP Biomedicals) at 6.0 m/s (3 × 30 s, 5 min pause time). After incubation at −80 °C for 1h, samples were centrifuged (10 min at 15,000×*g*, 4 °C), and supernatants (1.2 mL cell lysates) were transferred to fresh tubes and dried under a stream of nitrogen. Dried samples were reconstituted in 80 μL acetonitrile:methanol:water (2:2:1, v/v), vortexed for 5 min, centrifuged, and transferred to analytical glass vials. LC-MS grade water, acetonitrile, and methanol were obtained from Th. Geyer (Germany). The LC-MS/MS analysis was initiated within 1 h after the completion of the sample preparation.

LC-MS/MS analysis was performed on a Vanquish UHPLC system coupled to an Orbitrap Exploris 240 high-resolution mass spectrometer (Thermo Fisher Scientific) in negative ESI (electrospray ionization) mode, as previously described [26]. All experimental samples were measured in a randomized manner. Pooled quality control (QC) samples were prepared by mixing equal aliquots from each processed sample. Multiple QCs were injected at the beginning of the analysis to equilibrate the analytical system. A QC sample was analyzed after every 5th experimental sample to monitor instrument performance throughout the sequence. For the determination of background signals and subsequent background subtraction, an additional processed blank sample was recorded. Data was processed using MS-DIAL [27], and raw peak intensity data was exported. Feature identification was based on accurate mass, isotope pattern, MS/MS fragment scoring, and retention time matching to an in-house library. Normalization of the analyzed metabolites was performed on the cell number counted at the moment of the collection of the samples. Metabolites detected in less than 20 % of samples were filtered out. Missing values for the remaining metabolites were imputed using random draws from a Gaussian distribution centered at a minimal value with the impute LCMD v.2.1 Bioconductor package. Differential expression analysis was performed using limma v.3.54.1 Bioconductor package to obtain fold-change and p-values for each metabolite. P-values were adjusted for multiple tests using the Benjamini-Hochberg procedure to control the False Discovery Rate (FDR). Metabolites with an FDR <0.05 and a fold-change greater than 2 were considered modulated. Over-representation analysis (ORA) based on a hypergeometric test was conducted from the resulting list of modulated metabolites on the Kyoto Encyclopedia of Gene and Genomes (KEGG) database using fgsea v.1.24.0 Bioconductor package.

2.8. ^{13}C-based metabolic tracing

Cancer cells were seeded (2.5×10^5 cells/well; 3 wells/condition) in 6-well plates in routine culture medium for 24h. The day after, the medium was removed and replaced with culture medium (2 mL/well) containing 10 mM U-^{13}C glucose (#CIL-CLM-1396-2, LGC Standards) and 2 mM unlabeled glutamine or 10 mM unlabeled glucose and 2 mM U-^{13}C glutamine (#605166, Sigma-Aldrich) for 24h as well. The medium was then removed, and cells were washed with ice-cold NaCl 0.9 % solution before the addition of extraction buffer (300 μL methanol/well) and the incubation for 2–3 min on ice. Cells were then harvested using a cell scraper, and the extraction mix was transferred to a new microtube before centrifugation (15,000 rpm for 15 min at 4 °C). Finally, 250 μL of the supernatant (which contains intracellular metabolites) were transferred into a new microtube and stored at −80 °C until mass spectrometry analysis.

Each sample (10 μL) was loaded into a Dionex UltiMate 3000 LC System (Thermo Fisher Scientific) equipped with a C-18 column (Acquity UPLC -HSS T3 1. 8 μm; 2.1 × 150 mm, Waters) coupled to a Q Exactive Orbitrap mass spectrometer (Thermo Fisher Scientific) operating in negative ion mode. A step gradient was carried out using solvent A (10 mM TBA and 15 mM acetic acid) and solvent B (100 % methanol). The gradient started with 5 % of solvent B and 95 % of solvent A and remained at 5 % B until 2 min post injection. A linear gradient to 37 % B was carried out until 7 min and increased to 41 % until 14 min. Between 14 and 26 min, the gradient increased to 95 % of B and remained at 95 % B for 4 min. At 30 min, the gradient returned to 5 % B. The chromatography was stopped at 40 min. The flow was kept constant at 0.25 mL/min, and the column was placed at 40 °C throughout the analysis. The MS operated in full scan mode (m/z range: [70.0000–1050.0000]) using a spray voltage of 4.80 kV, a capillary temperature of 300 °C, sheath gas at 40.0, and auxiliary gas at 10.0. The AGC target was set at 3×10^6 using a resolution of 140000, with a maximum IT fill time of 512 ms. Data collection was performed using the Xcalibur software (Thermo Fisher Scientific). Data analyses were performed by integrating the peak areas (El-MAVEN – Polly - Elucidata).

2.9. 3D spheroid models

Spheroids were initiated and cultured as previously described [21]. Briefly, HT-29 cells (3×10^3 cells/well; ≥6 wells/condition) and HCT-116 cells (1.5×10^3 cells/well; ≥6 wells/condition) were seeded in

ultra-low attachment 96-well plates (Corning) in RPMI and DMEM respectively, supplemented with 10 % heat-inactivated FBS, 10 mM D-glucose and 2 mM L-glutamine. Spheroid growth was followed with daily picture acquisition by using an Axiovert 100 microscope (Zeiss) and area measurement using ImageJ 2.1.0/1.53c Java 1.8.0_172 (64-bit) software.

For immunofluorescence staining, OCT-embedded spheroids were cut into 5 μm slices using a cryostat CM1950 (Leica). Slides were incubated in 4 % PFA for 20 min at RT. Antigen retrieval was performed by immersing the slides in a mix of citrate buffer pH 6.8, Triton-X100, and water, with microwave cycles (4 min at 900W, 15 min at 90W, 90 s at 900W). The slides were then blocked with 5 % BSA in TTBS and subsequently incubated for 1h at RT with specific primary antibody against cleaved-caspase3 (#9661, Cell Signaling Technology, 1:200). Secondary antibody incubation with Envision^{+} system HRP-anti-rabbit (K4003, Dako) was carried out for 40 min at RT, followed by TSA amplification with fluorophore TSA CF647 (#96022, Biotium). Samples were stained with DAPI and prepared with a fluorescence mounting medium (Dako), before acquisition with an Axioscan Imager (Zeiss).

2.10. Patient-derived CRC organoids

CRC#2 organoid model was generated from colon cancer tissue obtained from a patient undergoing surgery at Cliniques Universitaires St Luc in Brussels (ethics committee approval ONCO-2015-02 updated on 13-05-2019 following the principles of the Declaration of Helsinki), as previously described [15]. Metastatic CRC organoid cultures (mCRC#327, #399, #534, and #1331) were obtained from a well-annotated living biobank at Candiolo Cancer Institute (Turin, Italy), containing patient-derived xenograft (PDX) models and PDX-derived organoids from patients with liver CRC metastatic lesions [28]. Signed informed consent was obtained from the patient before tumor collection and all personal/clinical data remained strictly confidential for the investigators. All CRC organoid cultures were plated in 50-μL domes of Cultrex Basement Membrane Extract, Type 2 (#3532-010-02, Bio-Techne) and maintained in Advanced DMEM/F12 (Thermo Fisher Scientific) supplemented with 1 % Glutamax (Thermo Fisher Scientific), 1 % HEPES (Thermo Fisher Scientific), 1 % penicillin-streptomycin (Thermo Fisher Scientific), 1 % B27 without vitamin A (Thermo Fisher Scientific), 1 % N2 supplement (Thermo Fisher Scientific), 50 ng/mL EGF, 10 mM nicotinamide (Sigma-Aldrich) and 1.25 mM N-acetyl cysteine (Sigma-Aldrich). Organoids were typically passaged every 7–10 days, and the medium was changed every 2–3 days. For splitting organoids, the medium was replaced with 500 μl Gentle Cell Dissociation Reagent (STEMCELL Technologies). The Cultrex dome was scraped and collected using a P1000 while pipetting up and down to break up the organoids and incubated on ice for 20 min before being centrifuged for 5 min at 400 g. The pellet was resuspended in an appropriate volume of Cultrex and plated in 50-μL domes in a 24-well plate (#3524, Costar, Corning). The plate was incubated at 37 °C for 15 min before adding 500 μL PDO medium.

Organoids were processed into single cells and seeded with a density of 5000 cells/5 μL Cultrex matrix per well in a 96-well plate. After 3–5 days, organoids acquired their typical 3D structure and were further treated with different concentrations of NCT-503 or IACS-010759 for 7 days. Cell viability was then assessed using the CellTiterGlo 3D Viability assay kit (G9682; Promega) by measuring ATP levels as luminescence with the GloMax plate reader (Promega). In parallel, after single-cell dissociation, organoids were seeded (4×10^4 cells per well) in 24 multi-well plates (Corning) embedded in the Cultrex matrix. After 3 days, organoids were treated with 5 μM NCT-503 or 10 nM IACS-010759 for 7 days. Organoids were then transferred into a μ-slide 8-well High Glass Bottom Ibidi chamber (#80841) for imaging purposes. To assess proliferation capacity, CRC organoids were incubated (4h at 37 °C) with Click-iT™ EdU Cell Proliferation Kit for Imaging, Alexa Fluor™ 647 dye (C10340; Thermo Fisher Scientific), according to manufacturer's recommendations, and then fixed with 4 % PFA for 1h at RT. The samples were further incubated in a permeabilization buffer composed of 0.2 % Triton-X100 and 1 % Tween-20 in TBS overnight at 4 °C. The following day, blocking with 5 % BSA in TTBS was performed, followed by overnight incubation with anti-Ki67 antibody (#MA5-14520, Invitrogen, 1:200) at 4 °C. Organoids were also stained with AlexaFluor-647 conjugated phalloidin (Thermo Fisher Scientific, 1:400). Samples were then washed and incubated with Hoechst 33258 (1:10,000), AlexaFluor-488 anti-rabbit secondary antibody (1:500) overnight at 4 °C. The day after, slides were prepared with a fluorescence mounting medium (Dako), and staining was visualized with a Zeiss Imager LSM800 confocal microscope (Zeiss).

For the CRC organoid live/dead staining, organoids were treated with the indicated drugs for 1 week. The culture medium was then withdrawn, and samples were washed with PBS three times. A 2X live-dead cell imaging solution (#R37601, Thermo Fisher Scientific) was prepared and added to the organoids after dilution in PBS. Subsequently, organoids were stained for 30 min at RT in the dark. Images were acquired with a Zeiss Axiovert S100 microscope, before analysis with ImageJ software (v.1.8.0).

2.11. Statistical analysis

Statistical analyses were performed with GraphPad Prism 10 software by using one-way or two-way ANOVA with Tukey's multiple comparison test when appropriate. Statistical significance is indicated in the figures as follows: $*p < 0.05$; $**p < 0.01$; $***p < 0.001$; ns, not significant.

2.12. Data and material availability

All unique reagents generated in this study will be made available on request by Prof. Cyril Corbet (cyril.corbet@uclouvain.be) with a completed material transfer agreement (MTA).

3. Results

3.1. Adaptation to chronic acidosis is associated with common metabolic alterations in molecularly heterogeneous CRC cells

To address the influence of chronic acidosis on CRC cell phenotypes, we first used four human CRC cell lines, namely DiFi, HCT-116, HT-29, and LIM1215, all harboring distinct *KRAS*, *NRAS*, *BRAF,* and *PIK3CA* gene alterations and MSI status (Fig. 1A) commonly observed in the patient population [29]. Importantly, all CRC cell lines exhibited different metabolic profiles at the basal level, as revealed by Seahorse-based bioenergetics analysis (Fig. 1B) and untargeted metabolomics (Fig. 1C). Of note, while HT-29 cells (with *BRAF* and *PIK3CA* activating mutations) were found to be the most glycolytic cell line, quadruple wild-type DiFi and LIM1215 cells showed a prevailing aerobic metabolism. HCT-116 cells displayed an "energetic" phenotype, with both mitochondrial respiration and glycolysis being active in these cells. All CRC cell lines were then chronically adapted to acidic extracellular pH (pH 6.5 vs pH 7.4 for control cell counterparts), as previously described [21–23], before metabolic characterization (Fig. 1D). Untargeted metabolomic analysis identified tens of down- or up-regulated metabolites ($\log_2$ FC < -1 or >1, respectively; FDR<0.05) between acidosis-adapted CRC cells and parental cell counterparts (Fig. 1E). Pathway enrichment analysis revealed alterations in several metabolic pathways, including amino acid metabolism, nucleotide metabolism, as well as glycolysis and gluconeogenesis (Supplementary Figs. S1A–D). Nevertheless, only four metabolites were found to be consistently up- (4-pyridoxic acid) or down-regulated (butyryl carnitine, lactic acid, and N-carbamoyl-DL-aspartic acid) in the four CRC cell lines under chronic acidic conditions (Fig. 1F). While 4-pyridoxic acid is a metabolite of vitamin B6, whose levels in serum samples from human patients were

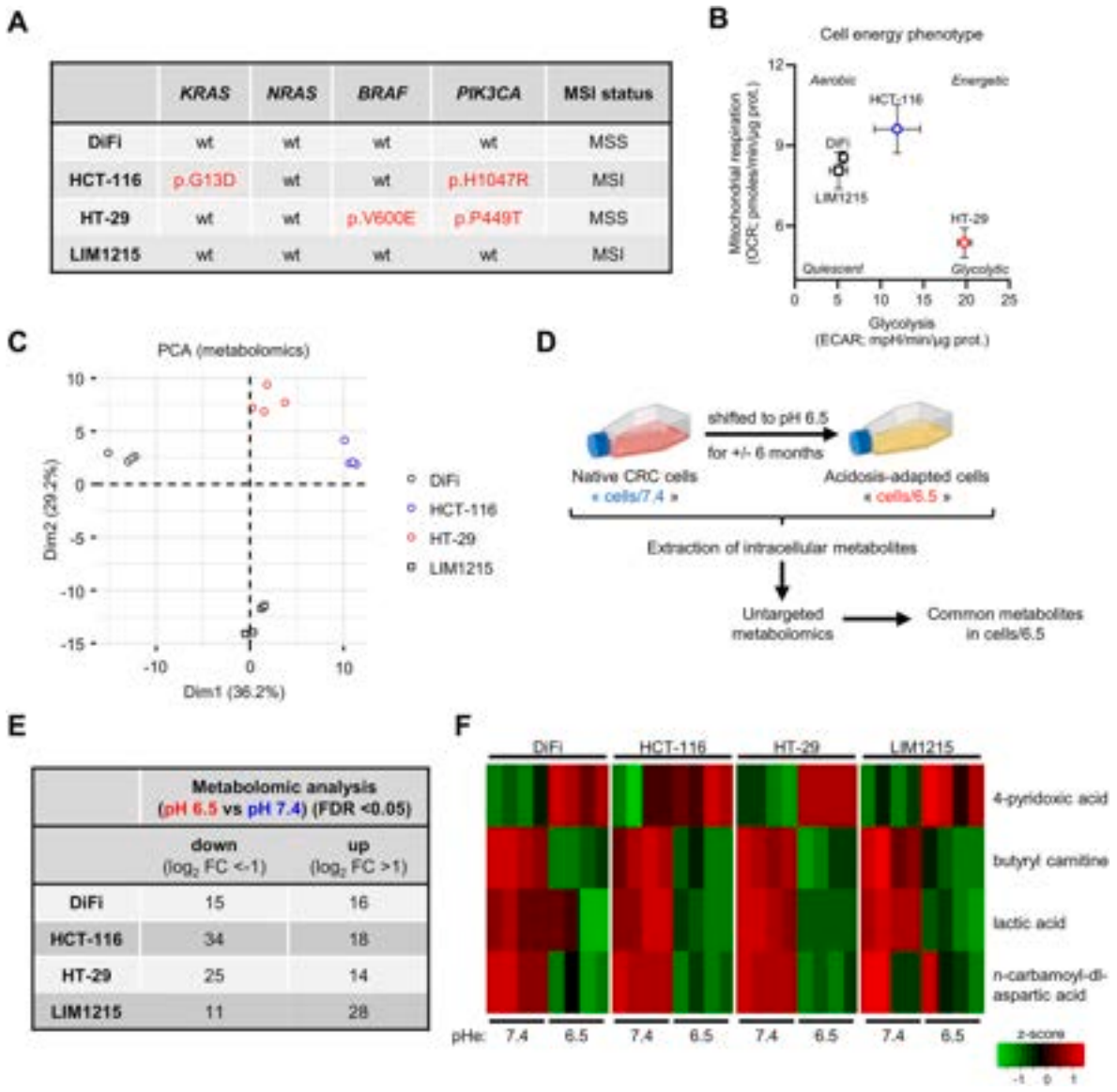

	KRAS	NRAS	BRAF	PIK3CA	MSI status
DiFi	wt	wt	wt	wt	MSS
HCT-116	p.G13D	wt	wt	p.H1047R	MSI
HT-29	wt	wt	p.V600E	p.P449T	MSS
LIM1215	wt	wt	wt	wt	MSI

	Metabolomic analysis (pH 6.5 vs pH 7.4) (FDR <0.05)	
	down (log_2 FC <-1)	up (log_2 FC >1)
DiFi	15	16
HCT-116	34	18
HT-29	25	14
LIM1215	11	28

Fig. 1. Adaptation to chronic acidosis is associated with common metabolic alterations in molecularly heterogeneous CRC cells. (**A**) Molecular characteristics of DiFi, HCT-116, HT-29, and LIM1215 CRC cell lines. MSS; microsatellite stability (**B**) Seahorse-based energetic profile (i.e., mitochondrial respiration vs glycolysis). of the different CRC cell lines after evaluation of basal oxygen consumption rates (OCR) and extracellular acidification rates (ECAR). (**C**) Principal component analysis of metabolomics data depicting the basal metabolic differences between the four CRC cell lines. (**D**) Experimental workflow for the metabolomic analysis carried out in native (pH7.4-exposed) and acidosis-adapted CRC cells. (**E**) Number of metabolites differentially up- or down-regulated in acidosis-adapted CRC cells (vs. native cells/7.4) and (**F**) heatmap of the commonly regulated metabolites in the four acidosis-adapted CRC cell populations. Data (**B-C** and **E-F**) were acquired from 2 independent cell cultures with 2 or 3 technical replicates.

associated with an increased lung cancer risk [30], butyryl carnitine is a butyrate ester of carnitine, previously reported to exert growth-inhibitory effects in CRC cells [31]. N-carbamoyl-DL-aspartic acid, also known as ureidosuccinic acid, serves as an intermediate in pyrimidine biosynthesis, and a drop in urinary levels for this metabolite was associated with bladder cancer [32]. Altogether, our data reveal that long-term exposure to extracellular acidosis can override, at least partly, the molecular heterogeneity in CRC cells to induce common metabolic alterations that may be further therapeutically exploited.

3.2. Glycolysis-to-respiration switch is a consistent metabolic adaptation in CRC cells under chronic acidosis

Downregulation of intracellular lactic acid levels, identified in the four acidosis-adapted CRC cell lines, is reminiscent of previous studies, including ours, reporting decreased glycolysis in tumor cells exposed to (long-term) acidic conditions [22,33]. To confirm that reduced glycolytic activity was a common metabolic trait in CRC cells exposed to chronic acidosis, regardless of their molecular background and basal metabolic profile, we first assessed, by mass spectrometry, the intracellular abundance of glycolytic intermediates, from hexose-6-phosphate to pyruvate and lactate. This analysis revealed that levels of most glycolysis-derived metabolites were consistently decreased in pH6.5-exposed CRC cells (Fig. 2A and Supplementary Figs. S2A–F). Importantly, this was associated with reduced glucose consumption and lactate secretion, as well as a decreased glucose-to-lactate ratio in all CRC cell populations under acidic culture conditions (Fig. 2B–D). Seahorse-based evaluation of extracellular acidification rates (ECAR; i.e. reflecting glycolytic activity through H^+ ion release) also showed that glucose-dependent and maximal ECAR values were lower in acidosis-adapted CRC cells (*vs* pH7.4-maintained parental cells) (Fig. 2E–I), thereby confirming that reduced glucose

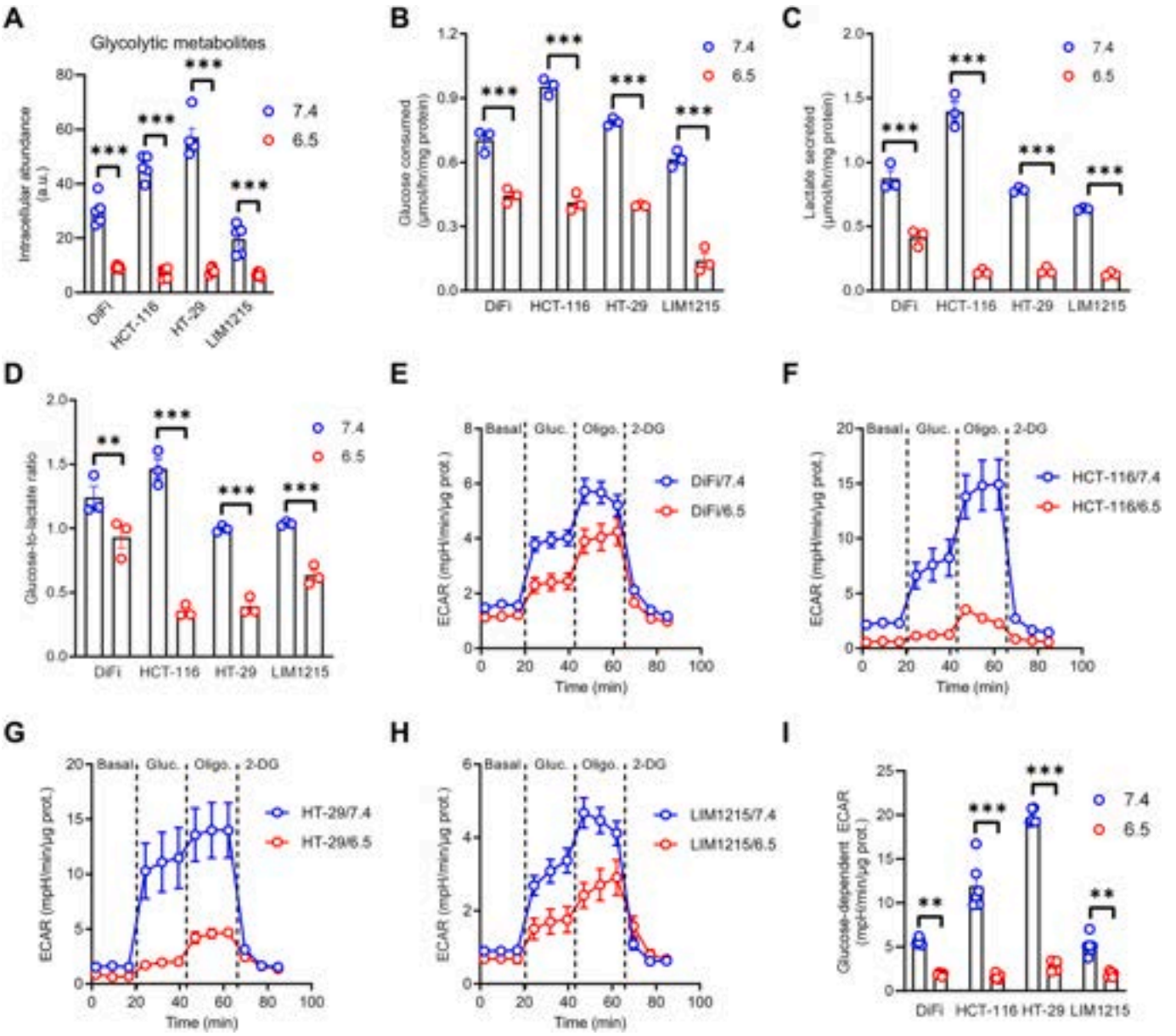

Fig. 2. Glycolytic activity is consistently decreased in CRC cells under chronic acidosis. (**A**) Intracellular levels of glycolytic metabolites in native and acidosis-adapted CRC cells. (**B-D**) Glucose consumption (**B**), lactate secretion (**C**), and glucose-to-lactate ratio (**D**) in native and acidosis-adapted CRC cells. (**E-H**) ECAR profile upon sequential treatment with 10 mM glucose, 1 µM oligomycin, and 50 mM 2-DG in native and acidosis-adapted DiFi (**E**), HCT-116 (**F**), HT-29 (**G**) and LIM1215 cells (**H**). (**I**) Glucose-dependent ECAR in native and acidosis-adapted CRC cells. Data are plotted as the means ± SEM from n = 3–4 cultures, performed each time with ≥3 technical replicates (**A-I**). Significance was determined by two-way ANOVA (**A-D** and **I**) with Tukey's multiple comparison test. **p < 0.01; ***p < 0.001.

metabolism towards lactate production/release was a common hallmark of CRC cells under chronic acidic conditions.

On the contrary, we observed that mitochondrial respiration was consistently increased in pH6.5-exposed CRC cells, in particular at maximal levels (i.e., upon treatment with the uncoupling agent FCCP in a medium containing 10 mM glucose and 2 mM glutamine to feed the tricarboxylic acid cycle) (Fig. 3A–C and Supplementary Figs. S3A–C). This was associated with greater growth-inhibitory effects in acidosis-adapted CRC cells (vs parental pH7.4-exposed CRC cells) upon treatment for 72h with 100 nM IACS-010759, a potent and specific inhibitor of mitochondrial respiratory complex I (Fig. 3D and E and Supplementary Figs. S3D–E). Importantly, we showed that IACS-010759 treatment was able to stimulate glycolytic activity (i.e. glucose consumption and lactate secretion) in pH6.5-exposed CRC cells, to an extent similar to that of parental cell counterparts (Fig. 3F–I and Supplementary Figs. S3F–I).

We also hypothesized that glutamine could play an anaplerotic role in acidosis-exposed CRC cells to sustain mitochondrial respiration. Seahorse-based bioenergetic analysis showed that, while glutamine-dependent OCR was increased in acidosis-adapted LIM1215 cells, it was not modified in the 3 other CRC cell models (Fig. 3J), thereby excluding a consistent metabolic change in CRC cells upon exposure to acidosis. Moreover, metabolic tracing analysis in CRC cells incubated with U-^{13}C-glutamine for 24h revealed that contribution of glutamine to TCA cycle intermediates (through its successive conversion into glutamate and then alpha-ketoglutarate) was not changed, and even decreased, in acidosis-adapted CRC cells, as shown with the percentage of labeling for glutamate, alpha-ketoglutarate (m+5), and succinate, fumarate, malate, aspartate, and citrate (m+4) through the oxidative metabolism of glutamine (Fig. 3K–M and Supplementary Figs. S3J–K). Altogether, our data show that acidosis-adapted CRC cells downregulate

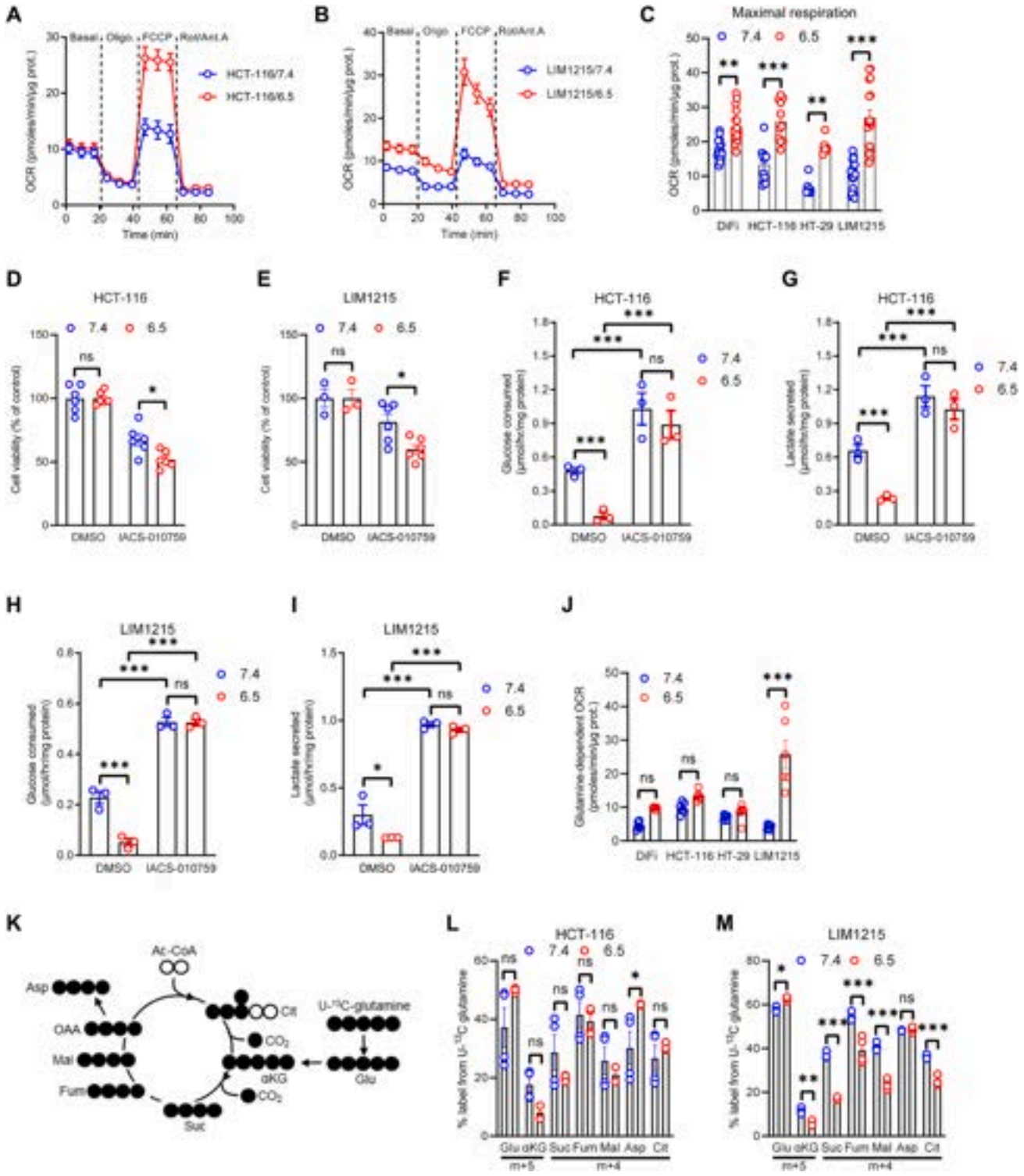

Fig. 3. Acidosis-adapted CRC cells rely on oxidative metabolism for their growth. (**A-B**) Oxygen consumption rates (OCR) upon sequential treatment with 1 μM oligomycin, 2 μM FCCP, and 0.5 μM rotenone/antimycin A in native and acidosis-adapted HCT-116 (**A**) and LIM1215 cells (**B**). (**C**) Maximal OCR values in native and acidosis-adapted CRC cells. (**D-E**) Viability of native and acidosis-adapted HCT-116 (**D**) and LIM1215 cells (**E**) upon treatment with 100 nM IACS-010759 for 72h. (**F-I**) Glucose consumption (**F** and **H**) and lactate secretion (**G** and **I**) for native and acidosis-adapted HCT-116 (**F-G**) and LIM1215 cells (**H-I**) upon treatment with 100 nM IACS-010759 for 24h. (**J**) Glutamine-dependent OCR in native and acidosis-adapted CRC cells. (**K**) Carbon atom transition map depicting labeling of TCA cycle intermediates (after one round) from [U-$^{13}C_5$]glutamine. (**L-M**) Relative abundance of glutaminolysis-specific mass isotopomers for glutamate (Glu), α-ketoglutarate (αKG), succinate (Suc), fumarate (Fum), malate (Mal), aspartate (Asp) and citrate (Cit) in native and acidosis-adapted HCT-116 (**L**) and LIM1215 cells (**M**) upon incubation with 2 mM [U-$^{13}C_5$]glutamine for 24h. Data are plotted as the means ± SEM from n = 3–4 cultures, performed each time with ≥3 technical replicates (**A-J** and **L-M**). Significance was determined by two-way ANOVA (**C-J** and **L-M**) with Tukey's multiple comparison test. *p < 0.05; **p < 0.01; ***p < 0.001; ns, not significant.

the glycolytic pathway and instead consistently become dependent on mitochondrial respiration to support their growth. Moreover, since oxidative phosphorylation (OXPHOS) inhibition with IACS-010759 triggers glycolysis stimulation in all CRC cell populations, regardless of the extracellular pH, we can exclude that acidosis-induced glycolysis downregulation relies on a defect in glycolytic enzymatic machinery or an incapacity to release lactate and H^+ ions against the physico-chemical gradient imposed when cells are incubated at pH 6.5.

3.3. PHGDH activity is indispensable for CRC cell viability under acidosis

To better assess the intracellular fate of glucose in acidosis-adapted CRC cells, we carried out metabolic tracing experiments on parental and acidosis-adapted CRC cells incubated for 24h with uniformly labeled ^{13}C-glucose (Fig. 4A). This analysis showed a lower ^{13}C labeling for most of the glycolytic intermediates (isotopomers m+6 or m+3), including hexose-(bi)phosphate, glyceraldehyde-3-phosphate (G3P), pyruvate and lactate in all pH6.5-exposed CRC cells (Fig. 4B–E and Supplementary Figs. S4A–D), thereby suggesting that glucose may be diverted towards alternative metabolic pathways. Interestingly, we observed that labeling for the m+3 isotopomer of serine (derived from 3-phosphoglycerate (3-PG) and subsequent activity of serine biosynthetic pathway (SBP) enzymes) was consistently increased in acidosis-adapted CRC cells (vs parental CRC cells) (Fig. 4F). This was associated with an increase in total intracellular levels of this amino acid in all pH6.5-exposed CRC cells (Fig. 4G), implying that glucose would be redirected towards the SBP to sustain CRC cell growth under chronic acidic conditions. Importantly, we could exclude a major role for glutamine metabolism in the production of serine since ^{13}C labeling in serine and glycine was undetectable or very weak (<0.5 %) in all CRC cell populations upon incubation with U-^{13}C-glutamine for 24h (Supplementary Figs. S4E–F).

To further explore the role of SBP in CRC cells under acidosis, we first assessed protein expression levels for the different enzymes involved in this pathway, namely phosphoglycerate dehydrogenase (PHGDH), phosphoserine aminotransferase 1 (PSAT1), phosphoserine phosphatase (PSPH), as well as serine hydroxymethyltransferases (SHMT) 1 and 2. Western blot analysis did not reveal any major and consistent protein expression change for PSPH, SHMT1, and SHMT2 in the different CRC cell populations (Supplementary Fig. S5A). On the contrary, PHGDH and PSAT1 followed the same expression pattern, with a downregulation in acidosis-adapted CRC cells (vs pH7.4-exposed parental cells), which was

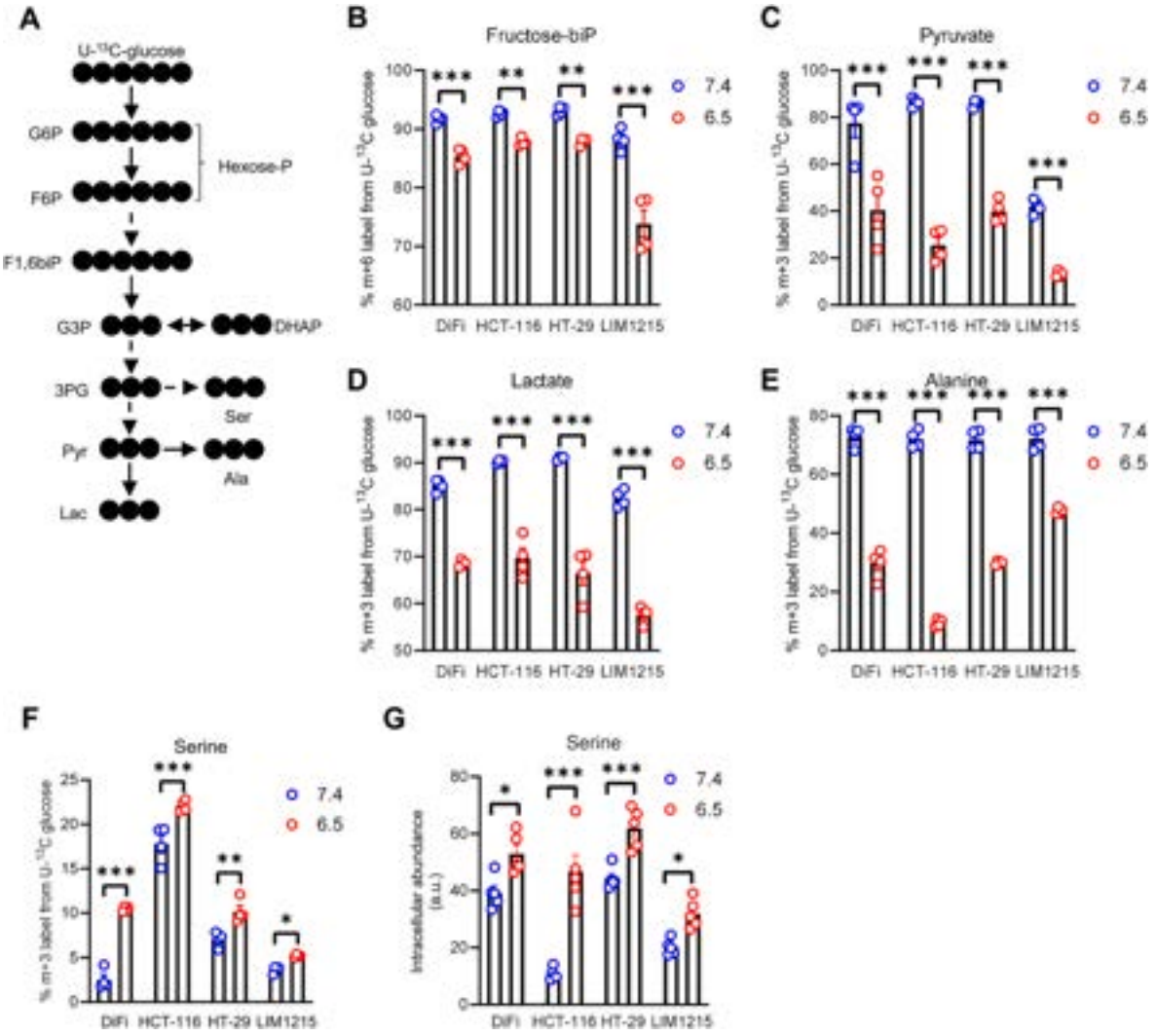

Fig. 4. Glucose is preferentially diverted towards serine biosynthesis pathway in acidosis-adapted CRC cells. (**A**) Carbon atom transition map depicting labeling of glycolytic intermediates and serine from [U-$^{13}C_6$]glucose. (**B-F**) Relative abundance of glycolysis-specific mass isotopomers for fructose-biphosphate (**B**), pyruvate (**C**), lactate (**D**), alanine (**E**), and serine (**F**) in native and acidosis-adapted CRC cells upon incubation with 10 mM [U-$^{13}C_6$]glucose for 24h. (**G**) Intracellular levels of serine in native and acidosis-adapted CRC cells. Data are plotted as the means ± SEM from n = 2 cultures, performed each time with 2 or 3 technical replicates (**B-G**). Significance was determined by two-way ANOVA (**B-G**) with Tukey's multiple comparison test. *p < 0.05; **p < 0.01; ***p < 0.001.

reversed when cancer cells were cultured back at pH 7.4 for 2 weeks (Supplementary Fig. S5A). Then, to evaluate the functional contribution of the SBP in acidosis-exposed CRC cells, we treated the different CRC cell populations with NCT-503, a potent and specific PHGDH inhibitor. We reported greater growth-inhibitory effects upon treatment for 72h with NCT-503 in all acidosis-adapted CRC cells (vs parental CRC cells) (Fig. 5A–D). Of note, a structurally-related inactive compound was also used as a negative control in those experiments and it did not show any major toxicity in CRC cells, even at the highest concentrations (Fig. 5A–D). Moreover, pharmacological treatment with CBR-5884, another PHGDH inhibitor, as well as siRNA-based genetic knock-down of PHGDH, exhibited similar cytotoxic effects specifically in acidosis-adapted CRC cells (Supplementary Figs. S5B–E), highlighting the importance of PHGDH enzymatic activity in those cell populations. Importantly, we also excluded the possibility that NCT503-induced specific cytotoxicity in pH6.5-exposed CRC cells was directly due to the extracellular pH by itself (i.e., change in protonation/activity state of the compound) rather than to an acidosis-driven metabolic cell phenotype. Indeed, when carrying out viability assays upon treatment with NCT-503 with pH6.5-adapted CRC cells cultured back at pH 7.4 only for

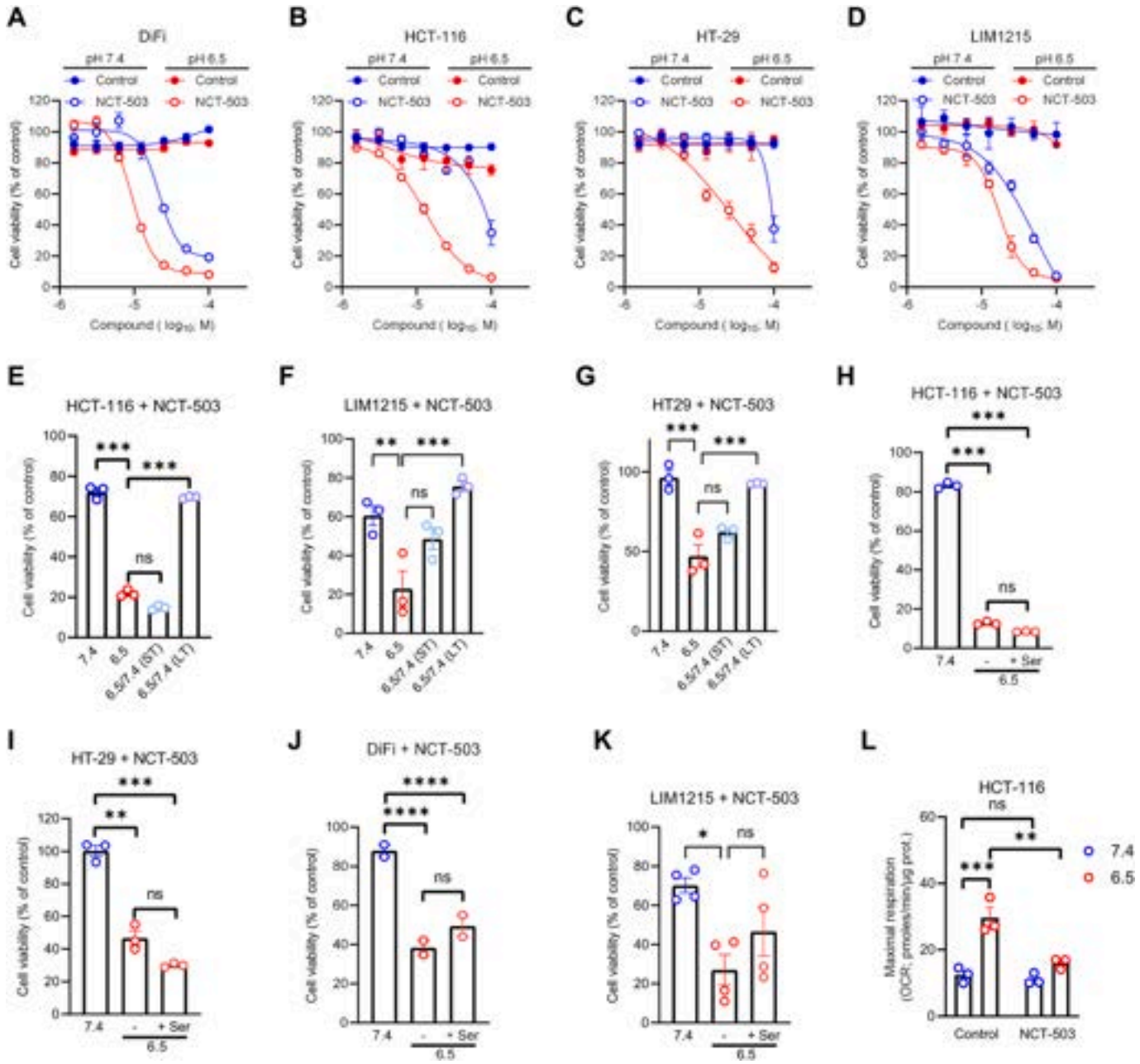

Fig. 5. PHGDH activity is indispensable for the growth of acidosis-adapted CRC cells. (**A-D**) Viability of native and acidosis-adapted DiFi (**A**), HCT-116 (**B**), HT-29 (**C**), and LIM1215 cells (**D**) after treatment with increasing concentrations of NCT-503 (or structurally-related inactive control) for 72h. (**E-G**) Viability of native and acidosis-adapted HCT-116 (**E**), LIM1215 (**F**), and HT29 cells (**G**) upon treatment with 50 μM NCT-503 in a culture medium buffered at pH 7.4 or 6.5. In some conditions, acidosis-adapted CRC cells were cultured back at pH 7.4 for short-term (ST; 72h) or long-term (LT; 2 weeks) periods. (**H-K**) Viability of native and acidosis-adapted HCT-116 (**H**), HT-29 (**I**), DiFi (**J**), and LIM1215 cells (**K**) upon treatment with 50 μM NCT-503 in a serine-containing or serine-deprived culture medium. (**L**) Oxygen consumption rates (OCR) at maximal levels (i.e., upon treatment with 2 μM FCCP) in native and acidosis-adapted HCT-116 cells upon treatment with 12.5 μM NCT-503 or vehicle for 24h. Data are plotted as means ± SEM from n = 3 cultures, performed each time with ≥3 technical replicates (**A-L**). Significance was determined by one-way ANOVA (**E-K**) or two-way ANOVA (**L**) with Tukey's multiple comparison test. *p < 0.05; **p < 0.01; ***p < 0.001; ns, not significant.

the 3 days of treatment (i.e., short-term (ST) incubation not sufficient to reverse the acidosis-induced metabolic phenotype, as previously reported [22,23]), PHGDH inhibition still triggered a dramatic growth inhibition in these cells (Fig. 5E-G). Instead, after culturing the pH6.5-adapted CRC cells back at pH 7.4 for 2 weeks (i.e., long-term (LT) incubation leading to metabolic phenotype reversal), NCT-503 effects on CRC cell growth were abolished (Fig. 5E–G and Supplementary Figs. S5F–H). Surprisingly, we also showed that medium supplementation with exogenous serine was not sufficient to rescue CRC cell viability upon PHGDH inhibition (Fig. 5H–K), thereby suggesting that the reliance of acidosis-adapted CRC cells on PHGDH enzymatic activity is not directly linked to the *de novo* serine synthesis. Interestingly, blockade of PHGDH enzyme activity also correlated with decreased maximal respiration rates in acidosis-adapted CRC cells treated with NCT-503 for 24h (Fig. 5L and Supplementary Figs. S5I–J). Importantly, in CRC cells cultured at physiological pH, NCT-503 treatment did not induce significant changes in OCR levels, thereby suggesting that PHGDH activity would be important to maintain mitochondrial respiratory capacity in CRC cells only when exposed to chronic acidosis.

3.4. 3D CRC cell models reveal spatially-resolved growth-inhibitory effects of OXPHOS and PHGDH inhibitors

In addition to imposing acidic pH culture conditions on 2D CRC cell monolayers via the use of HEPES/PIPES-buffered media, we also exploited 3D culture systems that naturally reproduce several physicochemical gradients, including nutrients, oxygen, and pH, to examine the growth-inhibitory effects of OXPHOS and PHGDH inhibitors. First, we generated 3D spheroids from HCT-116 and HT-29 CRC cells and treated them, 3 days post-initiation, with 100 nM IACS-010759 or 12.5 μM NCT-503 for 4 days. 7-day-old spheroids were further processed for immunostaining for cleaved caspase 3 as a marker of apoptotic cell death. Fluorescence microscopy analysis allowed us to reveal a spatial distribution of cleaved caspase 3 staining upon treatment of HT-29 spheroids with either IACS-010759 or NCT-503, with a greater fluorescent signal intensity in the core of the spheroids (*vs* the periphery) (Fig. 6A–E). Even though it was not statistically significant, a higher staining intensity for cleaved caspase 3 was also observed in inner regions from HCT-116 spheroids treated with OXPHOS or PHGDH inhibitors (Supplementary Fig. S6 A-E). In both spheroid models, staining was found to be more intense in internal regions (at ≈100 μm from the periphery) that correspond to areas where an acidic environment can naturally develop, as already reported [21]. These data suggest that CRC cells, located in inner (likely more acidic) regions of 3D spheroids, are more vulnerable to OXPHOS or PHGDH inhibition.

Finally, 3D patient-derived CRC organoids (PDO) were utilized to validate our initial observations in more complex and clinically relevant model systems. PDO models were derived from either primary colon tumors (pCRC#2) or CRC liver metastases (mCRC#327, #399, #534, and #1331) (Fig. 7A). We showed that both IACS-010759 and NCT-503 induced dose-dependent growth-inhibitory effects in all CRC PDO models (Fig. 7B and C). Brightfield images of CRC PDO models upon 1-week treatment with IACS-010759 or NCT-503 illustrated drug-induced cytotoxic effects with a significant alteration in the 3D architecture of the PDO cultures, regardless of their initial morphological shape (Fig. 7D). Remarkably, immunofluorescence analysis of CRC PDO models revealed a reduced proliferative activity, as indicated by the EdU marker (Fig. 7E) and Ki67 staining (Supplementary Fig. S7A) upon treatment with OXPHOS or PHGDH inhibitors. 3D PDO architecture was also impaired under treatment, as shown by phalloidin staining, which highlighted a more filamentous appearance under both treatments compared to the control condition (Supplementary Fig. S7A). Additionally, immunofluorescence staining with live and dead cell markers (calcein-AM and BOBO-3 iodide, respectively) revealed an increased cell death in CRC PDO models treated with IACS-010759 and NCT-503 compared to vehicle condition (Fig. 7F), thereby highlighting the

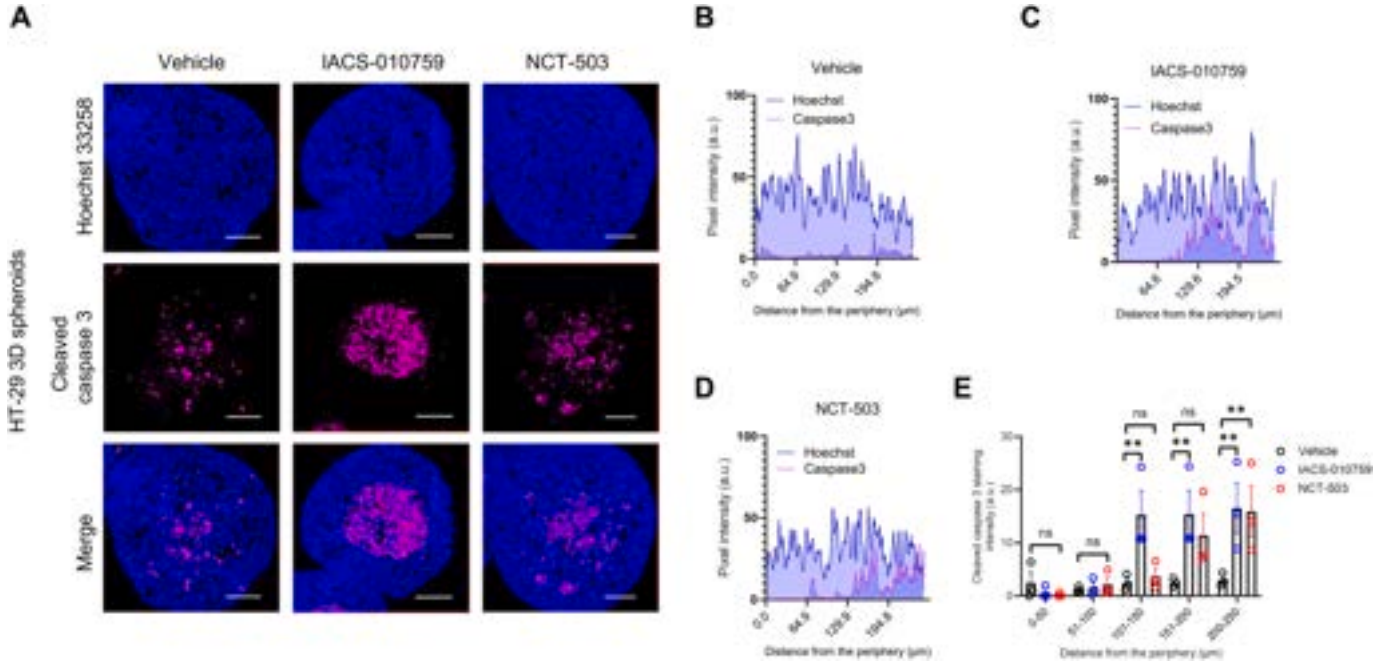

Fig. 6. Inhibition of OXPHOS or PHDGH activity induces greater growth-inhibitory effects in the acidic core of 3D CRC spheroids. (**A**) Representative immunofluorescence images for cleaved caspase 3 staining on slices from HT-29 spheroids upon treatment with 100 nM IACS-010759 or 12.5 μM NCT-503 for 96h. Magnification: 20×; scale bar: 100 μm. (**B-D**) Quantification of cleaved caspase 3 staining, indicated as pixel intensity, from the periphery of the spheroids towards the core in HT-29 spheroids treated with vehicle (**B**), 100 nM IACS-010759 (**C**) or 12.5 μM NCT-503 (**D**) for 96h. (**E**) Cleaved caspase 3 staining pixel intensities in different layers of HT-29 spheroids, starting from the periphery (0 μm) to the core of the 3D structure. Data are plotted as the means ± SEM from n = 3 cultures, performed each time with 2 technical replicates (**B-E**). Significance was determined by two-way ANOVA (**E**) with Tukey's multiple comparison test. **p < 0.01; ns, not significant.

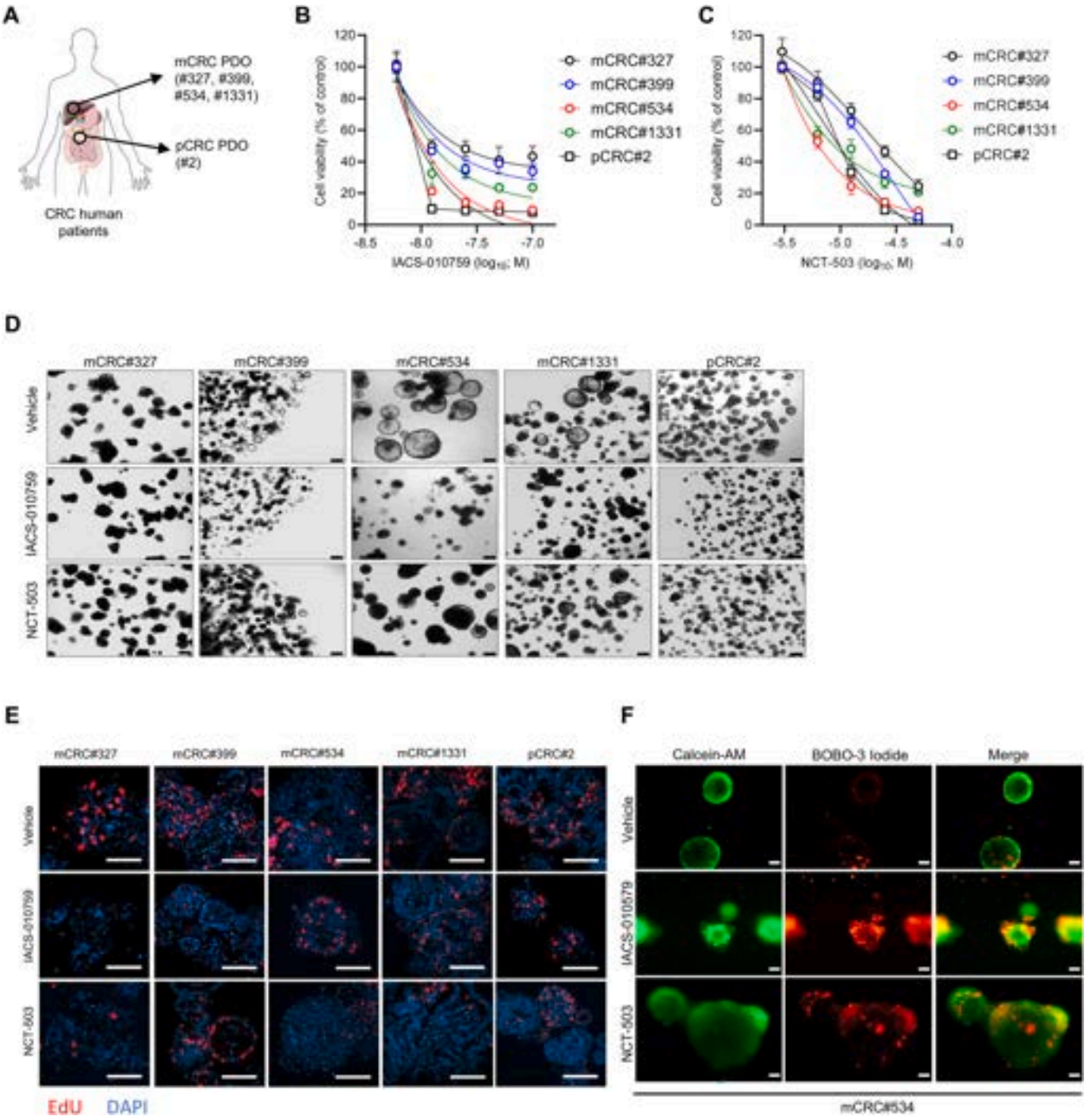

Fig. 7. Inhibition of OXPHOS or PHDGH activity triggers cytotoxic effects in patient-derived CRC organoids. (**A**) Drawing depicting the patient-derived CRC organoid models used in our study, originating from either primary colon tumor (pCRC#2) or CRC liver metastases (mCRC#327, #399, #534, #1331). (**B-C**) Viability of CRC PDO models after treatment with increasing concentrations of IACS-010759 (**B**) or NCT-503 (**C**) for 1 week. (**D**) Representative brightfield pictures of CRC PDO models after treatment with 5 μM NCT-503 or 10 nM IACS-010759 for 7 days. Magnification: 5×; scale bar: 100 μm. (**E**) Representative (immuno)fluorescence images for EdU (red) and DAPI (nuclear marker; blue) in CRC PDO models after treatment with 10 nM IACS-010759 or 5 μM NCT-503 for 7 days. Magnification: 20×; scale bar: 50 μm. (**F**) Representative fluorescence images for calcein-AM and BOBO-3 iodide staining in mCRC#534 PDO model after treatment with 10 nM IACS-010759 or 5 μM NCT-503 for 7 days. Magnification: 5×; scale bar: 200 μm. Data are plotted as the means ± SEM from n = 3 cultures, performed each time with 3 technical replicates (**B-C**). (For interpretation of the references to colour in this figure legend, the reader is referred to the Web version of this article.)

therapeutic potential of these drugs in preclinical models of CRC.

4. Discussion

According to the Darwinian nature of cancer, besides genetic instability, highly selective local microenvironments (the so-called niches) are thought to help the development of adaptive phenotypes in tumor cells to sustain malignant progression and support therapeutic failures [34]. For instance, along with cancer progression, metabolic acidosis (i.e., local accumulation of H^+ ions) is one of the major

microenvironmental selection barriers that tumor cell populations must surmount to sustain disease development [35,36]. Acidosis largely arises from the conjunction of the exacerbated metabolism of cancer cells (and cancer-associated cells) with a spatio-temporal disorganization of the tumor vasculature that limits access to O_2 and prevents the rapid elimination of waste products, including protons. Many studies have reported therapeutic approaches to target tumor acidosis, ranging from direct neutralization of tumor-derived acid with systemic buffers [37], use of inhibitors for H^+ and HCO_3^--handling proteins [38] to the administration of pH-sensitive drug delivery systems [39]. In addition, several groups, including ours, have shown that exploiting acidosis-induced metabolic vulnerabilities may also represent a new strategy to target this specific tumor cell compartment and reduce disease progression, including therapy resistance and metastatic dissemination [40]. Nevertheless, it remains unclear whether the molecular heterogeneity of tumor cells may impact the effectiveness of metabolism-interfering treatments aiming at killing acidosis-exposed tumor cells.

Here, by using a panel of CRC cell lines harboring distinct molecular features, including the presence of *KRAS*, *BRAF*, *PIK3CA* activating gene mutations, and MSS or MSI status, we first revealed a consistent downregulation of glycolysis in all CRC cells in favor of an increase of mitochondrial respiration and serine metabolic pathways, upon long-term exposure to acidic pH conditions. Our findings parallel earlier observations delineating the pronounced impact of acidosis, as opposed to hypoxia, on the metabolic and transcriptomic profiles exhibited by cancer cells [17,41,42]. Indeed, OXPHOS was shown to be increased under acidic conditions with a parallel reduction of the glycolytic potential in a variety of tumor types, including glioblastoma, and liver and lung cancers [43–45]. In particular, *NDUFS1*, among other OXPHOS-related genes, proved to be essential for the survival of cancer cells under acidic conditions [46]. Importantly, we reported specific growth-inhibitory effects for IACS-010759, a potent inhibitor of the electron transport chain complex I, towards acidosis-exposed CRC cells in 2D culture models but also in more complex systems such as 3D spheroids and patient-derived tumor organoids in which gradients for oxygen, pH, and nutrients naturally develop, thereby making these systems suitable for metabolic studies [47]. An obvious explanation behind the glycolysis-to-respiration in cancer cells exposed to acidic conditions resides in the limited capacity to release glycolysis-derived lactate and H+ ions against their concentration gradients, forcing them to turn to preferentially mitochondrial metabolism. Nevertheless, we cannot exclude that the phenotypic advantage of an OXPHOS-dependent metabolic phenotype goes beyond the bioenergetic/biosynthetic supply, as it may also be linked to other phenotypic changes, including epigenetic modifications.

In this study, we also identified a glucose diversion towards the SBP, leading to a metabolic dependency on the enzymatic activity of PHGDH in acidosis-exposed CRC cells. Increased SBP activity has been associated with poor prognosis in CRC patients [48], and linked to an increase in purine biosynthesis and better response to 5-FU-induced DNA damage [49]. While genetic and pharmacological targeting of PHGDH led to growth inhibition specifically in acidosis-exposed CRC cells, its functional role remains poorly understood. Indeed, supplementation with extracellular serine failed to rescue CRC cell viability upon PHGDH inhibition, suggesting an alternative function of the enzyme. In several studies, PHGDH has been associated with alternative roles beyond its canonical function in serine production, in particular by increasing mitochondrial respiration. In breast cancers, PHGDH suppression did not affect intracellular serine levels but resulted in a deficiency in anaplerosis of glutamine to αKG [50]. Another recent study shed light on a non-canonical activity of PHGDH and its role in liver cancer growth via increased mitochondrial translation and respiratory metabolism [51]. Nuclear translocation of PHGDH has also been linked to reduced NAD^+ levels and repression of c-Jun PARylation and transcriptional activity in the nucleus, thereby leading to tumor growth under nutrient stress-induced conditions [52]. Altogether, these observations suggest that increased PHGDH activity and mitochondrial respiration may be intricately connected to support CRC cell growth under acidic conditions.

From a therapeutic perspective, the identification of cellular metabolism as a critical adaptation mechanism to therapy- and microenvironment-induced stress conditions in cancer cells created a new field of investigation for the development of new antitumor compounds aiming at preventing disease progression [53–55]. Nevertheless, metabolic plasticity and flexibility capacities in cancer cells usually lead to quick adaptive responses, thereby preventing the use of metabolism-interfering strategies as monotherapies. For instance, several PHGDH inhibitors have been developed and used in preclinical studies but they have not reached clinical application yet [56]. Moreover, results from a phase I clinical trial revealed that IACS-010759 showed very disappointing outcomes in cancer patients, with a narrow therapeutic index associated with intolerable neurotoxicity, despite initially promising preclinical findings [57,58].

To conclude, our findings raise the possibility of therapeutically targeting, individually or in combination, mitochondrial metabolism and the serine biosynthesis pathway as new cancer treatment options to kill some of the most aggressive cancer cell subpopulations, located in acidic regions within the tumor bulk, delay tumor progression, and improve response to conventional anticancer treatments.

CRediT authorship contribution statement

Elena Richiardone: Writing – original draft, Investigation, Formal analysis, Data curation, Conceptualization. **Maria Virginia Giolito:** Investigation, Formal analysis. **Rim Al Roumi:** Investigation, Formal analysis. **Jérôme Ambroise:** Methodology, Formal analysis, Data curation. **Romain Boidot:** Methodology. **Bernhard Drotleff:** Methodology. **Bart Ghesquière:** Methodology. **Barbara Lupo:** Resources. **Livio Trusolino:** Resources. **Alberto Bardelli:** Resources. **Sabrina Arena:** Methodology, Formal analysis. **Olivier Feron:** Supervision, Resources, Funding acquisition. **Cyril Corbet:** Writing – original draft, Supervision, Resources, Funding acquisition, Formal analysis, Data curation.

Conflict of interest statement

S.A. reports personal fees from MSD Italia and a patent (Italian patent application No. 102022000007535) outside the submitted work. A.B. reports receipt of grants/research support from Neophore, AstraZeneca, and Boehringer Ingelheim and honoraria/consultation fees from Guardant Health. A.B. is a stock shareholder of Neophore and Kither Biotech. A.B. is an advisory board member for Neophore. L.T. reports research grants from Menarini, Merck KGaA, Merus, Pfizer, Servier, and Symphogen outside the submitted work. The other authors declare no competing interests.

Declaration of competing interest

The authors declare the following financial interests/personal relationships which may be considered as potential competing interests: S. A. reports personal fees from MSD Italia and a patent (Italian patent application No. 102022000007535) outside the submitted work. A.B. reports receipt of grants/research support from Neophore, AstraZeneca, and Boehringer Ingelheim and honoraria/consultation fees from Guardant Health. A.B. is a stock shareholder of Neophore and Kither Biotech. A.B. is an advisory board member for Neophore. L.T. reports research grants from Menarini, Merck KGaA, Merus, Pfizer, Servier, and Symphogen outside the submitted work. The other authors declare no competing interests.

Acknowledgments

This work has been supported by research grants from the Fonds National de la Recherche Scientifique (F.R.S.-FNRS), the Belgian Foundation against Cancer, the J. Maisin Foundation, and the Walloon Region through the FRFS WELBIO strategic research program (C.C.). Research grants AIRC (Associazione Italiana per la Ricerca sul Cancro) under IG 2023 - ID. 28922 project; PRIN 2022 - Prot. 2022CHB9BA financed by European Union - Next Generation EU (A.B.) have been obtained by A.B. S.A. has also received funding from AIRC IG 2023- ID 29286 project, MUR Dipartimento di Eccellenza 2023–2027 14586 DIORAMA, Finanziamento dell'Unione Europea NextGeneration EU M4 C2 investimento 1.1.- PRIN 2022 PNRR P2022E3BTH, FPRC 5x1000 Ministero della Salute 2022 CARESS, and Italian Ministry of Health, Ricerca Corrente 2024. This work has also been supported by funding to L.T. from AIRC, Investigator Grant; AIRC 5 × 1000 grant 21091; AIRC/CRUK/FC AECC Accelerator Award 22795; Italian Ministry of University and Research, National Recovery and Resilience Plan, project PNC0000001; Fondazione Piemontese per la Ricerca sul Cancro-ONLUS, 5 × 1000 Ministero della Salute 2016 and 2022. CC is a FNRS Research Associate and Principal Investigator at the WEL Research Institute. ER and R.AR are FNRS-FRIA PhD fellows.

Appendix A. Supplementary data

Supplementary data to this article can be found online at https://doi.org/10.1016/j.canlet.2025.217512.

References

[1] R.L. Siegel, N.S. Wagle, A. Cercek, R.A. Smith, A. Jemal, Colorectal cancer statistics, 2023, CA Cancer J Clin 73 (3) (2023) 233–254.
[2] F. Di Nicolantonio, P.P. Vitiello, S. Marsoni, S. Siena, J. Tabernero, L. Trusolino, et al., Precision oncology in metastatic colorectal cancer - from biology to medicine, Nat. Rev. Clin. Oncol. 18 (8) (2021) 506–525.
[3] A. Cervantes, R. Adam, S. Rosello, D. Arnold, N. Normanno, J. Taieb, et al., Metastatic colorectal cancer: ESMO Clinical Practice Guideline for diagnosis, treatment and follow-up, Ann. Oncol. 34 (1) (2023) 10–32.
[4] J. Guinney, R. Dienstmann, X. Wang, A. de Reynies, A. Schlicker, C. Soneson, et al., The consensus molecular subtypes of colorectal cancer, Nat Med 21 (11) (2015) 1350–1356.
[5] D.K.H. Chan, S.J.A. Buczacki, Tumour heterogeneity and evolutionary dynamics in colorectal cancer, Oncogenesis 10 (7) (2021) 53.
[6] P. Dalerba, T. Kalisky, D. Sahoo, P.S. Rajendran, M.E. Rothenberg, A.A. Leyrat, et al., Single-cell dissection of transcriptional heterogeneity in human colon tumors, Nat. Biotechnol. 29 (12) (2011) 1120–1127.
[7] I. Joanito, P. Wirapati, N. Zhao, Z. Nawaz, G. Yeo, F. Lee, et al., Single-cell and bulk transcriptome sequencing identifies two epithelial tumor cell states and refines the consensus molecular classification of colorectal cancer, Nat. Genet. 54 (7) (2022) 963–975.
[8] S.F. Roerink, N. Sasaki, H. Lee-Six, M.D. Young, L.B. Alexandrov, S. Behjati, et al., Intra-tumour diversification in colorectal cancer at the single-cell level, Nature 556 (7702) (2018) 457–462.
[9] F. Wang, J. Long, L. Li, Z.X. Wu, T.T. Da, X.Q. Wang, et al., Single-cell and spatial transcriptome analysis reveals the cellular heterogeneity of liver metastatic colorectal cancer, Sci. Adv. 9 (24) (2023) eadf5464.
[10] X. Wu, H. Yan, M. Qiu, X. Qu, J. Wang, S. Xu, et al., Comprehensive characterization of tumor microenvironment in colorectal cancer via molecular analysis, Elife 12 (2023).
[11] J. Yun, C. Rago, I. Cheong, R. Pagliarini, P. Angenendt, H. Rajagopalan, et al., Glucose deprivation contributes to the development of KRAS pathway mutations in tumor cells, Science 325 (5947) (2009) 1555–1559.
[12] G. Huang, T. Zhao, C. Wang, K. Nham, Y. Xiong, X. Gao, et al., PET imaging of occult tumours by temporal integration of tumour-acidosis signals from pH-sensitive (64)Cu-labelled polymers, Nat. Biomed. Eng. 4 (3) (2020) 314–324.
[13] F.J. Voskuil, P.J. Steinkamp, T. Zhao, B. van der Vegt, M. Koller, J.J. Doff, et al., Exploiting metabolic acidosis in solid cancers using a tumor-agnostic pH-activatable nanoprobe for fluorescence-guided surgery, Nat. Commun. 11 (1) (2020) 3257.
[14] T. Zhao, G. Huang, Y. Li, S. Yang, S. Ramezani, Z. Lin, et al., A Transistor-like pH nanoprobe for tumour detection and image-guided surgery, Nat. Biomed. Eng. 1 (2016).
[15] L. Aubert, E. Bastien, O. Renoult, C. Guilbaud, K. Ozkan, D. Brusa, et al., Tumor acidosis-induced DNA damage response and tetraploidy enhance sensitivity to ATM and ATR inhibitors, EMBO Rep. 25 (3) (2024) 1469–1489.
[16] T. Morita, T. Nagaki, I. Fukuda, K. Okumura, Clastogenicity of low pH to various cultured mammalian cells, Mutat. Res. 268 (2) (1992) 297–305.
[17] J.L. Chen, J.E. Lucas, T. Schroeder, S. Mori, J. Wu, J. Nevins, et al., The genomic analysis of lactic acidosis and acidosis response in human cancers, PLoS Genet. 4 (12) (2008) e1000293.
[18] E. Andreucci, S. Peppicelli, J. Ruzzolini, F. Bianchini, A. Biagioni, L. Papucci, et al., The acidic tumor microenvironment drives a stem-like phenotype in melanoma cells, J. Mol. Med. (Berl.) 98 (10) (2020) 1431–1446.
[19] C. Vander Linden, C. Corbet, Therapeutic targeting of cancer stem cells: integrating and exploiting the acidic niche, Front. Oncol. 9 (2019) 159.
[20] J.W. Wojtkowiak, J.M. Rothberg, V. Kumar, K.J. Schramm, E. Haller, J. B. Proemsey, et al., Chronic autophagy is a cellular adaptation to tumor acidic pH microenvironments, Cancer Res. 72 (16) (2012) 3938–3947.
[21] C. Corbet, E. Bastien, J.P. Santiago de Jesus, E. Dierge, R. Martherus, C. Vander Linden, et al., TGFbeta2-induced formation of lipid droplets supports acidosis-driven EMT and the metastatic spreading of cancer cells, Nat. Commun. 11 (1) (2020) 454.
[22] C. Corbet, N. Draoui, F. Polet, A. Pinto, X. Drozak, O. Riant, et al., The SIRT1/HIF2alpha axis drives reductive glutamine metabolism under chronic acidosis and alters tumor response to therapy, Cancer Res. 74 (19) (2014) 5507–5519.
[23] C. Corbet, A. Pinto, R. Martherus, J.P. Santiago de Jesus, F. Polet, O. Feron, Acidosis drives the reprogramming of fatty acid metabolism in cancer cells through changes in mitochondrial and histone acetylation, Cell Metab. 24 (2) (2016) 311–323.
[24] M.G. Rolver, L.K.K. Holland, M. Ponniah, N.S. Prasad, J. Yao, J. Schnipper, et al., Chronic acidosis rewires cancer cell metabolism through PPARalpha signaling, Int. J. Cancer 152 (8) (2023) 1668–1684.
[25] R.H. Whitehead, F.A. Macrae, D.J. St John, J. Ma, A colon cancer cell line (LIM1215) derived from a patient with inherited nonpolyposis colorectal cancer, J Natl Cancer Inst 74 (4) (1985) 759–765.
[26] E. Richiardone, Roumi R. Al, F. Lardinois, M.V. Giolito, J. Ambroise, R. Boidot, et al., MCT1-dependent lactate recycling is a metabolic vulnerability in colorectal cancer cells upon acquired resistance to anti-EGFR targeted therapy, Cancer Lett. 598 (2024) 217091.
[27] H. Tsugawa, T. Cajka, T. Kind, Y. Ma, B. Higgins, K. Ikeda, et al., MS-DIAL: data-independent MS/MS deconvolution for comprehensive metabolome analysis, Nat. Methods 12 (6) (2015) 523–526.
[28] S.M. Leto, E. Grassi, M. Avolio, V. Vurchio, F. Cottino, M. Ferri, et al., XENTURION is a population-level multidimensional resource of xenografts and tumoroids from metastatic colorectal cancer patients, Nat. Commun. 15 (1) (2024) 7495.
[29] E. Medico, M. Russo, G. Picco, C. Cancelliere, E. Valtorta, G. Corti, et al., The molecular landscape of colorectal cancer cell lines unveils clinically actionable kinase targets, Nat. Commun. 6 (2015) 7002.
[30] H. Zuo, P.M. Ueland, O. Midttun, S.E. Vollset, G.S. Tell, D. Theofylaktopoulou, et al., Results from the European prospective investigation into cancer and nutrition link vitamin B6 catabolism and lung cancer risk, Cancer Res. 78 (1) (2018) 302–308.
[31] M.J. Roy, S. Dionne, G. Marx, I. Qureshi, D. Sarma, E. Levy, et al., In vitro studies on the inhibition of colon cancer by butyrate and carnitine, Nutrition 25 (11–12) (2009) 1193–1201.
[32] C. Shen, Z. Sun, D. Chen, X. Su, J. Jiang, G. Li, et al., Developing urinary metabolomic signatures as early bladder cancer diagnostic markers, OMICS 19 (1) (2015) 1–11.
[33] G. Lamonte, X. Tang, J.L. Chen, J. Wu, C.K. Ding, M.M. Keenan, et al., Acidosis induces reprogramming of cellular metabolism to mitigate oxidative stress, Cancer Metab 1 (1) (2013) 23.
[34] R.J. Gillies, D. Verduzco, R.A. Gatenby, Evolutionary dynamics of carcinogenesis and why targeted therapy does not work, Nat. Rev. Cancer 12 (7) (2012) 487–493.
[35] C. Corbet, O. Feron, Tumour acidosis: from the passenger to the driver's seat, Nat. Rev. Cancer 17 (10) (2017) 577–593.
[36] P. Swietach, E. Boedtkjer, S.F. Pedersen, How protons pave the way to aggressive cancers, Nat. Rev. Cancer 23 (12) (2023) 825–841.
[37] A. Ibrahim-Hashim, D. Abrahams, P.M. Enriquez-Navas, K. Luddy, R.A. Gatenby, R. J. Gillies, Tris-base buffer: a promising new inhibitor for cancer progression and metastasis, Cancer Med. 6 (7) (2017) 1720–1729.
[38] A. Bogdanov, A. Bogdanov, V. Chubenko, N. Volkov, F. Moiseenko, V. Moiseyenko, Tumor acidity: from hallmark of cancer to target of treatment, Front. Oncol. 12 (2022) 979154.
[39] M. Deskeuvre, J. Lan, E. Dierge, J. Messens, O. Riant, C. Corbet, et al., Targeting cancer cells in acidosis with conjugates between the carnitine palmitoyltransferase 1 inhibitor etomoxir and pH (low) insertion peptides, Int J Pharm 624 (2022) 122041.
[40] E. Dierge, E. Debock, C. Guilbaud, C. Corbet, E. Mignolet, L. Mignard, et al., Peroxidation of n-3 and n-6 polyunsaturated fatty acids in the acidic tumor environment leads to ferroptosis-mediated anticancer effects, Cell Metab. 33 (8) (2021) 1701, 17015 e5.
[41] M. Khacho, M. Tarabay, D. Patten, P. Khacho, J.G. MacLaurin, J. Guadagno, et al., Acidosis overrides oxygen deprivation to maintain mitochondrial function and cell survival, Nat. Commun. 5 (2014) 3550.
[42] X. Tang, J.E. Lucas, J.L. Chen, G. LaMonte, J. Wu, M.C. Wang, et al., Functional interaction between responses to lactic acidosis and hypoxia regulates genomic transcriptional outputs, Cancer Res. 72 (2) (2012) 491–502.
[43] K. Duan, Z.J. Liu, S.Q. Hu, H.Y. Huo, Z.R. Xu, J.F. Ruan, et al., Lactic acid induces lactate transport and glycolysis/OXPHOS interconversion in glioblastoma, Biochem. Biophys. Res. Commun. 503 (2) (2018) 888–894.
[44] H. Wu, M. Ying, X. Hu, Lactic acidosis switches cancer cells from aerobic glycolysis back to dominant oxidative phosphorylation, Oncotarget 7 (26) (2016) 40621–40629.

[45] S. Zeng, X. Hu, Lactic acidosis switches cancer cells from dependence on glycolysis to OXPHOS and renders them highly sensitive to OXPHOS inhibitors, Biochem. Biophys. Res. Commun. 671 (2023) 46–57.
[46] J. Michl, Y. Wang, S. Monterisi, W. Blaszczak, R. Beveridge, E.M. Bridges, et al., CRISPR-Cas9 screen identifies oxidative phosphorylation as essential for cancer cell survival at low extracellular pH, Cell Rep. 38 (10) (2022) 110493.
[47] E. Richiardone, V. Van den Bossche, C. Corbet, Metabolic studies in organoids: current applications, opportunities and challenges, Organoids 1 (1) (2022) 85–105.
[48] X.Q. Jia, S. Zhang, H.J. Zhu, W. Wang, J.H. Zhu, X.D. Wang, et al., Increased expression of PHGDH and prognostic significance in colorectal cancer, Transl Oncol 9 (3) (2016) 191–196.
[49] E. Pranzini, E. Pardella, L. Muccillo, A. Leo, I. Nesi, A. Santi, et al., SHMT2-mediated mitochondrial serine metabolism drives 5-FU resistance by fueling nucleotide biosynthesis, Cell Rep. 40 (7) (2022) 111233.
[50] R. Possemato, K.M. Marks, Y.D. Shaul, M.E. Pacold, D. Kim, K. Birsoy, et al., Functional genomics reveal that the serine synthesis pathway is essential in breast cancer, Nature 476 (7360) (2011) 346–350.
[51] Y. Shu, Y. Hao, J. Feng, H. Liu, S.T. Li, J. Feng, et al., Non-canonical phosphoglycerate dehydrogenase activity promotes liver cancer growth via mitochondrial translation and respiratory metabolism, EMBO J. 41 (23) (2022) e111550.
[52] C. Ma, K. Zheng, K. Jiang, Q. Zhao, N. Sha, W. Wang, et al., The alternative activity of nuclear PHGDH contributes to tumour growth under nutrient stress, Nat. Metab. 3 (10) (2021) 1357–1371.
[53] Z.E. Stine, Z.T. Schug, J.M. Salvino, C.V. Dang, Targeting cancer metabolism in the era of precision oncology, Nat. Rev. Drug Discov. 21 (2) (2022) 141–162.
[54] Y. Xiao, T.J. Yu, Y. Xu, R. Ding, Y.P. Wang, Y.Z. Jiang, et al., Emerging therapies in cancer metabolism, Cell Metab. 35 (8) (2023) 1283–1303.
[55] A.C. Goncalves, E. Richiardone, J. Jorge, B. Polonia, C.P.R. Xavier, I.C. Salaroglio, et al., Impact of cancer metabolism on therapy resistance - clinical implications, Drug Resist Updat 59 (2021) 100797.
[56] C.M. Lee, Y. Hwang, M. Kim, Y.C. Park, H. Kim, S. Fang, PHGDH: a novel therapeutic target in cancer, Exp. Mol. Med. 56 (7) (2024) 1513–1522.
[57] T.A. Yap, N. Daver, M. Mahendra, J. Zhang, C. Kamiya-Matsuoka, F. Meric-Bernstam, et al., Complex I inhibitor of oxidative phosphorylation in advanced solid tumors and acute myeloid leukemia: phase I trials, Nat Med 29 (1) (2023) 115–126.
[58] X. Zhang, C.V. Dang, Time to hit pause on mitochondria-targeting cancer therapies, Nat Med 29 (1) (2023) 29–30.